Laser-induced persistent orientation of chiral molecules

Ilia Tutunnikov,[1] Johannes Floß,[2] Erez Gershnabel,[1] Paul Brumer,[2,*] and Ilya Sh. Averbukh[1,†]
[1]*AMOS and Department of Chemical and Biological Physics, Weizmann Institute of Science, Rehovot 7610001, Israel*
[2]*Chemical Physics Theory Group, Department of Chemistry, and Center for Quantum Information and Quantum Control, University of Toronto, Toronto, Ontario, Canada M5S 3H6*

(Received 16 July 2019; published 14 October 2019)

We study, both classically and quantum mechanically, enantioselective orientation of gas-phase chiral molecules excited by laser fields with twisted polarization. Counterintuitively, the induced orientation, whose direction is laser controllable, does not disappear after the excitation but stays long after the end of the laser pulses. We computationally demonstrate this long-lasting orientation, using propylene oxide molecules (CH_3CHCH_2O, or PPO) as an example, and consider two kinds of fields with twisted polarization: a pair of delayed cross-polarized pulses and an optical centrifuge. This chiral effect opens avenues for detecting molecular chirality, measuring enantiomeric excess, and separating enantiomers with the help of inhomogeneous external fields.

DOI: 10.1103/PhysRevA.100.043406

I. INTRODUCTION

Chiral molecules exist in two enantiomeric forms. The two enantiomers are mirror images of each other, and they are nonsuperimposable by translation and rotation [1]. Molecular chirality is an omnipresent natural phenomenon of extreme importance in physics, chemistry, and biology [2]. The ability to discriminate and separate mixtures of enantiomers is important, for example, in drug synthesis, as different enantiomers of chiral drugs may exhibit strikingly different biological activity.

The related studies of gas-phase chiral molecules focus on the measurements of enantiomeric excess, handedness of a given compound, and on devising techniques for manipulating mixtures containing both enantiomers [3–24]. In addition, over the years more ambitious directions were considered theoretically—laser-assisted asymmetric synthesis, enantiomeric interconversion, and purification (e.g., [3,25] and references therein).

Recently, a pair of nonresonant delayed cross-polarized laser pulses was proposed as a tool for discrimination of chiral molecules [26–28] and the underlying classical enantioselective molecular orientation mechanism was revealed [27,28]. The approach was extended to general fields with time-dependent polarization twisting in a plane. Optical fields with fixed linear polarization are unable to induce molecular orientation because of the symmetry of light interaction with the induced dipole. Polarization twisting in a certain plane breaks that symmetry and defines a preferred spatial direction perpendicular to that plane that depends on the sense of polarization rotation. When interacting with molecules, the twisted field has a twofold effect. First, it induces unidirectional rotation (UDR) of the most polarizable molecular axis in the plane of polarization twisting [29–34], thereby orienting the averaged angular momentum vector $\langle \boldsymbol{\ell} \rangle$ perpendicular to the plane. In addition, in the case of chiral molecules, the twisted field induces an orienting torque *along* the most polarizable axis, thus orienting the molecule itself perpendicular to the aforementioned plane [27,28]. The direction of orientation depends on both the sense of polarization twisting and the handedness of the molecule. A pair of delayed cross-polarized laser pulses [29,30] provides the simplest example of the field with twisted polarization, but there are also more complex fields, such as chiral pulse trains [35–37], polarization-shaped pulses [38–40], and optical centrifuge [41–45]. Most recently, the orientation of chiral propylene oxide (PPO) molecules by means of an optical centrifuge was experimentally achieved in [46], thus providing the first demonstration of enantioselective laser control over molecular rotation.

In this paper, we concentrate on the long-term behavior of the enantioselective molecular orientation by twisted fields, which was noted to persist long after the end of the excitation [27,28]. Using the tools of classical mechanics, we discuss the conditions required for persistent orientation in an ensemble of asymmetric tops. As an example, we analyze a simplified model of an ensemble of chiral PPO molecules excited by a pair of cross-polarized short laser pulses, which is shown to satisfy the conditions for persistent orientation. Moreover, we carry out fully quantum simulations of a PPO molecule driven by fields with twisted polarization. Quantum treatment provides access to timescales far exceeding the ones during which the classical analysis is valid, and it shows that orientation of chiral molecules remains long-lived in the quantum regime. On the short timescale, the quantum and classical simulations are in complete agreement. Two implementations of the laser fields with twisted polarization are considered—a pair of delayed cross-polarized pulses and an optical centrifuge. The laser-induced orientation is shown to be robust against normally detrimental temperature effects.

*paul.brumer@utoronto.ca
†ilya.averbukh@weizmann.ac.il

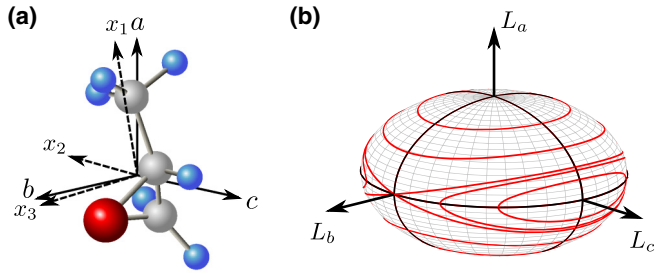

FIG. 1. (a) (*R*)-propylene oxide molecule. Atoms are color-coded: gray - carbon, blue - hydrogen, red - oxygen. Principal axes of inertia tensor are shown as solid arrows and denoted by a, b, and c ($I_a < I_b < I_c$), while those of the polarizability tensor are shown as dashed arrows and denoted by x_1, x_2, and x_3 ($\alpha_{33} < \alpha_{22} < \alpha_{11}$). (b) Binet ellipsoid, where red indicates the allowed trajectories of the angular momentum vector.

The paper is organized as follows. In Sec. II, using the classical mechanics analysis, the conditions needed for long-lasting field-free orientation in a pulse-excited ensemble of classical molecules are discussed, and we show that chiral molecules excited by a laser field with twisted polarization satisfy these conditions. In Sec. III, the results of classical and fully quantum simulations of the enantioselective orientation at thermal conditions are provided. Section IV concludes the paper.

II. CLASSICAL ANALYSIS

In this section we use classical mechanics to analyze conditions leading to the existence of permanent orientation in a gas of field-free rotating asymmetric-top molecules. We show that excitation of an isotropic ensemble of chiral molecules by twisted fields satisfies these conditions.

Background. The Binet construction [47,48] allows us to classify the trajectories traversed by the angular momentum vector in the molecule-fixed frame defined by the three principal axes of moment of inertia tensor. Figure 1(a) shows one of the enantiomers [right handed, (*R*)] of our example molecule, propylene oxide (CH_3CHCH_2O, or PPO), with two sets of axes: principal axes of moment of inertia and polarizability tensors. Hereafter, the letters a, b, c refer to the inertia principal frame, whereas the numbers 1, 2, 3 refer to the polarizability principal frame.

We briefly describe the construction. Free motion of an asymmetric-top rotor has four constants of motion, energy, and the three components of angular momentum expressed in an inertial frame (laboratory-fixed frame). In the frame of principal axes of the inertia tensor [see Fig. 1(a)], the allowed trajectories of the angular momentum vector satisfy the following equations:

$$\frac{L_a^2}{2EI_a}+\frac{L_b^2}{2EI_b}+\frac{L_c^2}{2EI_c}=1, \quad \frac{L_a^2+L_b^2+L_c^2}{L^2}=1, \qquad (1)$$

where I_j are the moments of inertia, L_j are the components of the angular momentum vector ($j=a,b,c$), E is the rotational energy, and L is the magnitude of the angular momentum vector. The moments of inertia are ordered according to $I_a < I_b < I_c$. The first expression defines an ellipsoid with semiaxes $\sqrt{2EI_a}$, $\sqrt{2EI_b}$, and $\sqrt{2EI_c}$; these coincide with the principal axes of the inertia tensor. The second expression defines a spherical shell with radius L. The angular momentum vector tip moves on the ellipsoid-spherical shell intersections. In addition to the six stationary rotations about each of the three inertia tensor principal axes, the allowed trajectories can be divided into sets of closed curves, as shown in Fig. 1(b).

For $\sqrt{2EI_a} < L < \sqrt{2EI_b}$ and $\sqrt{2EI_b} < L < \sqrt{2EI_c}$, the trajectories are divided into two sets of curves T_k ($k=a,c$) enclosing the poles on the a and c axes, respectively [see Fig. 1(b)]. The sign of L_k is conserved on these trajectories, and depending on the enclosed pole (either on positive or negative side of the axis), we denote the corresponding sets by $T_k^{\pm}$. Although the Binet construction provides a qualitative picture of $\mathbf{L}$ trajectories, as seen from the molecule-fixed frame, it allows us to deduce some valuable information about the motion in the laboratory frame as well. In the case of a single top, we can assume that the conserved vector of angular momentum $\boldsymbol{\ell}$ points along the laboratory Z axis. For definiteness, we assume T_c trajectory, meaning that $\mathbf{L}$ moves on a "taco-shaped" curve around one of the poles on the c axis [see Fig. 1(b)]. This implies that in the laboratory frame the c axis "precesses" around $\boldsymbol{\ell}$ while the sign of the projection $\hat{\mathbf{c}}\cdot\hat{\boldsymbol{\ell}} = \hat{\mathbf{c}}\cdot\hat{\mathbf{Z}}$ remains unchanged, which means preferred orientation of the c axis in the course of time. Notably, even in the case of an ensemble of asymmetric tops, i.e., when initially angular momenta vectors point in various directions, the permanent orientation is still possible. In that case permanent orientation corresponds to the ensemble-averaged quantities $\langle\hat{\mathbf{a}}\cdot\hat{\mathbf{Z}}\rangle$ or $\langle\hat{\mathbf{c}}\cdot\hat{\mathbf{Z}}\rangle$ having a constant sign. This may be achieved by, first, orienting the averaged angular momentum vector $\langle\boldsymbol{\ell}\rangle$ (e.g., along Z axis) and, second, breaking the symmetry between T_k^+ vs T_k^- trajectories.

Particular case of twisted polarization. Here we consider a specific example of an ensemble of chiral molecules excited by pair of delayed cross-polarized laser pulses [29–31], which constitutes the simplest implementation of a field with twisted polarization. We show that such an excitation leads to the conditions discussed above. Here, the first pulse is polarized along the laboratory X axis, while the polarization of the second one is in the XY plane at $+\pi/4$ to the X axis. The first pulse induces alignment of the most polarizable molecular axis. For the sake of simplicity of the qualitative analysis, we assume that after the first pulse all the molecules are perfectly aligned along the X axis and are stationary [27]. Initially, we consider only half of all molecules, in which the most polarizable axis points along $+X$ [see Fig. 2(a)]. Angle $\varphi\in[0,2\pi)$ is the angle between the Y axis and the x_2 axis, lying in the YZ plane [see Fig. 2(b)]. The aligned molecules are uniformly distributed in φ. The interaction potential U and torque $\mathbf{T}$ induced by a nonresonant optical field are given by

$$U=-\tfrac{1}{2}\langle\mathbf{d}_{\rm ind}\cdot\mathbf{E}\rangle \quad \mathbf{T}=\langle\mathbf{d}_{\rm ind}\times\mathbf{E}\rangle\,, \qquad (2)$$

where the angle brackets denote time averaging over the optical cycle, $\mathbf{d}_{\rm ind}=\boldsymbol{\alpha}\mathbf{E}$ is the induced dipole, $\boldsymbol{\alpha}$ is the polarizability tensor, and $\mathbf{E}$ is the vector of the electric field. The interaction with a permanent molecular dipole vanishes, because the optical fields (having typical frequency 10^{14} Hz) considered in this work are far detuned from any dipole

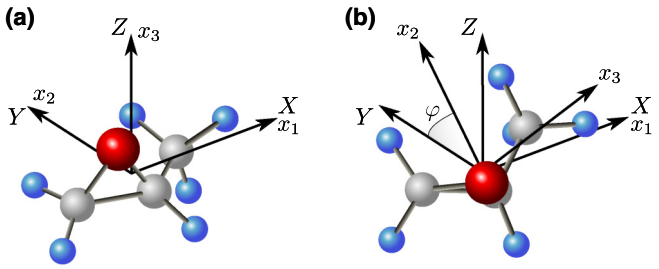

FIG. 2. (a) The frame of polarizability principal axes x_1, x_2, and x_3 ($\alpha_{33} < \alpha_{22} < \alpha_{11}$) coincides with the laboratory-fixed frame. (b) The molecule is rotated (about X) by an angle φ, measured from the positive Y axis to positive x_2 axis, lying in the YZ plane.

transitions (having typical frequency 10^{11} Hz). The duration of the laser pulses is assumed to be short as compared to the typical rotational periods of the chiral molecules; therefore the effect of the second pulse is considered in the impulsive approximation, $\Delta\mathbf{L} \propto \mathbf{T}$, where $\Delta\mathbf{L}$ is the sudden change in the angular momentum of a molecule.

The second pulse (twisted with respect to the first one) induces unidirectional rotation in the XY plane, resulting in orientation of $\langle\boldsymbol{\ell}\rangle$ along Z, which constitutes the first criterion for the long-lasting orientation. In addition, there is an orienting torque acting on the aligned most polarizable axis, x_1. To check whether the second criterion for the long-lasting orientation is satisfied, we evaluate the torques along the molecular a and c axes, τ_k ($k = a, c$),

$$\tau_k \propto C_k \sin(2\varphi) + D_k \sin(\varphi + \phi_k), \tag{3}$$

where $C_k = (\alpha_{33} - \alpha_{22})R_{k1}/2$, $D_k = \sqrt{A_k^2 + B_k^2}$, $A_k = (\alpha_{11} - \alpha_{33})R_{k2}$, $B_k = (\alpha_{11} - \alpha_{22})R_{k3}$, and $\tan(\phi_k) = B_k/A_k$. Here, R_{nm} are the elements of the orthogonal rotation matrix relating the principal polarizability and inertia frames (see Appendix A for details). For a chiral molecule, the two frames do not align [see Fig. 1(a)] and the off-diagonal elements of R differ from zero. In this case, the subdomains of positive and negative τ_k in the interval $\varphi \in [0, 2\pi)$ are not equal, which is precisely the required T_k^+ vs T_k^- asymmetry. When the two frames do align (as in nonchiral molecules), R becomes diagonal, resulting in torques $\tau_a = C_a \sin(2\varphi)$ and $\tau_c = A_c \sin(\varphi)$. In this case, the T_k^+ vs T_k^- symmetry is preserved.

It may be shown that Eq. (3) remains the same for molecules with the most polarizable axis, x_1 pointing along $-X$. For the complimentary enantiomer [(*S*)-PPO], signs of some of the elements of R_{nm} are reversed, resulting in the opposite orientation direction (see Appendix A for details).

III. NUMERICAL SIMULATIONS

In this section, we present the results of numerical simulations of the laser-driven orientation dynamics of (*R*)-PPO molecules. We consider two implementations of laser fields with twisted polarization, a pair of delayed cross-polarized pulses [29–31] and an optical centrifuge [41–45]. The behavior of an ensemble of $N \gg 1$ molecules is investigated using both classical and quantum-mechanical tools. The chiral molecule is modeled as a rigid asymmetric top having anisotropic polarizability and a dipole moment. Table I summarizes the molecular parameters of (*R*)-PPO used in our simulations.

For the classical simulations, the behavior of a thermal ensemble was simulated using the Monte Carlo approach. Our numerical scheme relies on solving the Euler equations for angular velocities and parametrizing the rotations by quaternions [50]. The details of the scheme may be found in [28]. Before the excitation, the molecules are isotropically distributed, and the angular velocities are assigned according to the Boltzmann distribution for a given temperature.

For the quantum simulations, we use the symmetric top wave functions $|JKM\rangle$ as a basis set [51]. Here J is the total angular momentum (in Section II we used the label L for the modulus of the classical angular momentum), K is its projection on the molecule-fixed c axis, and M is its projection onto the laboratory-fixed Z axis. In this basis, the matrix representing the kinetic energy Hamiltonian has a tridiagonal form in which the states of different K's are coupled with $K \pm 2$ states [see Eq. (B3)]. The interaction potential is expressed in terms of Wigner D-matrices, and its matrix elements are evaluated in the $|JKM\rangle$ basis. The explicit expressions used may be found in Appendix B. Then, a unitary transformation is applied, transforming the matrices to the asymmetric-top basis, in which the kinetic energy Hamiltonian becomes diagonal. All the thermally populated (for a given temperature) eigenstates of the chiral molecule are propagated in time separately, and thermal averaging is performed to obtain the observables of interest. The explicit expressions for matrix elements of the observables are presented in Appendix B as well.

Double-pulse excitation. Here we consider excitation of an ensemble of (*R*)-PPO molecules by a pair of delayed cross-polarized laser pulses. The first pulse is polarized along the laboratory X axis, while the polarization of the second one is in the XY plane at $+\pi/4$ angle to the X axis. The electric field of the pulses is given by

TABLE I. Summary of molecular properties: eigenvalues of the moment of inertia tensor (atomic units), components of polarizability tensor (atomic units), and components of dipole moment (Debye) in the body-fixed frame of molecular principal axes. For the complimentary enantiomers, the values of α_{ac}, α_{bc}, and μ_c have the opposite sign. The molecular electronic properties were computed using the GAUSSIAN software package (method: CAM-B3LYP/aug-cc-pVTZ) [49].

Molecule	Moments of inertia	Polarizability tensor components	Dipole moment components
(R)-PPO	$I_a = 180386$ $I_b = 493185$ $I_c = 553513$	$\alpha_{aa} = 45.63$, $\alpha_{ab} = 2.56$ $\alpha_{bb} = 37.96$, $\alpha_{ac} = 0.85$ $\alpha_{cc} = 37.87$, $\alpha_{bc} = 0.65$	$\mu_a = 0.965$ $\mu_b = -1.733$ $\mu_c = 0.489$

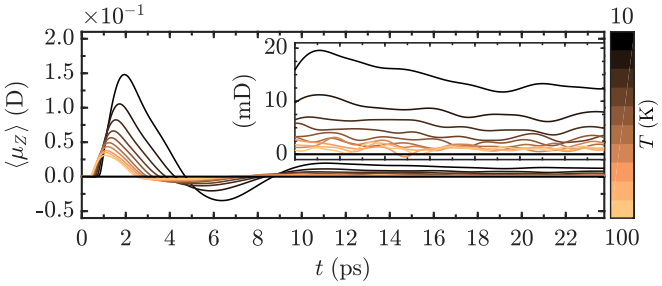

FIG. 3. Classical simulation of ensemble-averaged projection of the molecular dipole on the Z axis $\langle\mu_Z\rangle(t)$ for the case of (R)-PPO molecules excited by a pair of cross-polarized pulses. Here $N = 6 \times 10^6$. The curves span the range of temperatures from 10 (black) to 100 K (copper/light gray) in steps of 10 K. Parameters of the pulses are $I_0 = 0.5 \times 10^{14}$ W/cm^2, FWHM = 100 fs. The first pulse is centered at $t = 0$, while the delay of the second pulse is optimized for each temperature value (see text). Horizontal line is set at $\langle\mu_Z\rangle = 0$. The inset is an amplified version of the figure.

$\boldsymbol{\mathcal{E}}_i(t) = \mathcal{E}_0 \exp[-2\ln 2(t - t_j)^2/\tau_0^2]\cos(\omega t)\mathbf{e}_i$, where $\mathcal{E}_0$ is the maximal amplitude of the electric field of the pulse, τ_0 is the FWHM of the intensity profile, ω is the carrier frequency of the pulse, and $\mathbf{e}_i$ is a unit vector along the polarization direction ($i = 1, 2$). The maximal amplitude of the electric field is related to the peak intensity by $I_0 = \varepsilon_0 c E_0^2/2$, where ε_0 is the permittivity of vacuum and c is the speed of light in vacuum.

The simulated classical results span the range of temperatures $T \in [10, 100]$ K with a step of 10 K. The first pulse leads to the alignment of the most polarizable molecular axis along X, and the second pulse is applied when this alignment reaches the maximal value. Since this value as well as the time required to reach it are temperature dependent, the moment of application of the second pulse was optimized for each temperature.

Figure 3 shows the ensemble-averaged projection of the molecular dipole on the Z axis as a function of time, $\langle\mu\rangle(t)$ resulting from excitation by both pulses. As may be seen, the second pulse results in a sharp transient orientation of the ensemble-averaged dipole, reaching an approximately constant value in the long term. It is important to emphasize that the orientation direction is perpendicular to the plane of twisting and its sign depends on both the sense of twisting and the handedness of the molecule. The sign of orientation is opposite for the second enantiomer (S)-PPO. The classical mechanism explaining the induced enantioselective transient orientation is described elsewhere [27,28]. The maximal amplitudes of both the transient and the persistent dipole are temperature dependent and become lower with increasing the temperature. The long-lasting dipole signals shown in Fig. 3 exhibit small-amplitude beats about the asymptotically constant values. These beats stem from the statistical nature of the simulations, and their amplitude is inversely proportional to $\sqrt{N}$.

To access the influence of the quantum effects on the permanent orientation, we carried out fully quantum-mechanical simulations of the dynamics of (R)-PPO molecules kicked by the two pulses. The pulse envelope used in the quantum simulations is given by Eq. (B1). The difference between this

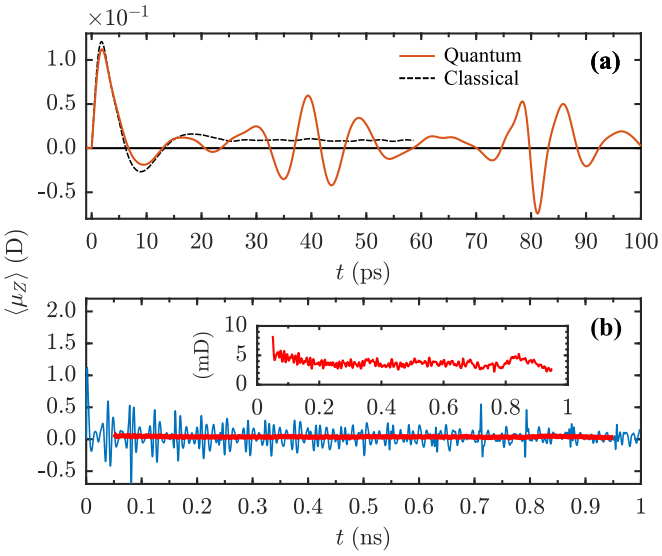

FIG. 4. Quantum expectation value of projection of the molecular dipole on the Z axis $\langle\mu_Z\rangle(t)$ for the case of (R)-PPO molecules excited by a pair of cross-polarized pulses. The temperature is set at $T = 5$ K. Parameters of the pulses are $I_0 = 1.43 \times 10^{14}$ W/cm^2, FWHM = 20 fs. The first pulse is centered at $t = 0$, and the delay of the second pulse is 1.2 ps. (a) The short-time dipole signal (solid) and its classical counterpart (dashed). (b) Blue (gray) indicates long-time dynamics, and red (black) the 100-ps time average, $\overline{\langle\mu_Z\rangle(t)} = (\Delta t)^{-1}\int_{t-\Delta t/2}^{t+\Delta t/2}\langle\mu_Z\rangle(t')dt'$. Inset is a magnified portion of the figure.

envelope and the Gaussian one used in the classical simulation is insignificant, as the pulses are short and the difference in their integrals is negligible (<1%). The rotational temperature was set to $T = 5$ K. The delay of the second pulse was adjusted to the moment of maximal alignment of the most polarizable axis towards the X axis, as measured using the alignment factor [see Eq. (B18)]. Depending on the initial conditions, the pulses excite the molecules to the states with J up to $20\hbar$ with the mean value of about $8\hbar$, which is above the average thermal value of $3.5\hbar$. The short-time dipole signal [see Eq. (B13)] is shown in Fig. 4(a) with its classical counterpart for comparison. Shortly after the pulse, the polarization peaks at about 0.12 D. In contrast to the classically predicted permanent steady-state dipole signal, the quantum curve exhibits beats spaced by ≈40 ps (the first few). These quantum beats are a well-known phenomenon for quantum rotors [52]. However, the long-term time-averaged signal differs from zero, see Fig. 4(b). The inset of the figure shows the time average as defined in the figure's caption.

Optical centrifuge excitation. An optical centrifuge is a laser pulse whose linear polarization undergoes an accelerated rotation around its propagation direction [41–45]. We model the electric field of such a pulse by

$$\boldsymbol{\mathcal{E}} = \varepsilon(t)[\cos(\beta t^2)\mathbf{e}_X + \sin(\beta t^2)\mathbf{e}_Y]\cos(\omega t), \qquad (4)$$

where β is the angular acceleration and $\varepsilon(t)$ is the envelope (dashed curve, Figs. 5 and 6); for explicit expression see Eq. (B2). As in the previous case, we start with the results of the classical simulations. Figure 5 shows the ensemble-averaged projection of the molecular dipole on the Z axis as

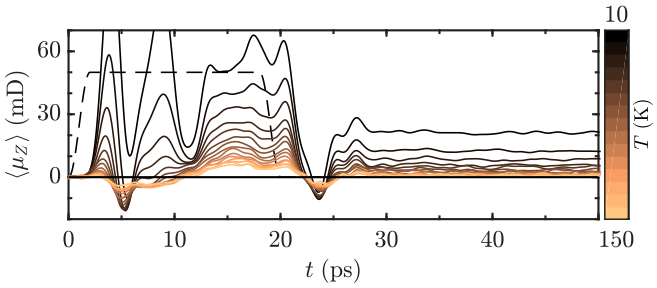

FIG. 5. Classical simulation of ensemble-averaged projection of the molecular dipole on the Z axis $\langle \mu_Z \rangle (t)$ for the case of (R)-PPO molecules excited by the optical centrifuge. The curves span the range of temperatures from 10 (black) to 150 K (copper/light gray) in steps of 10 K. Here $N = 9 \times 10^6$. Parameters of the pulse are $I_0 = 5 \times 10^{12}$ W/cm^2, $\beta = 0.065$ ps^{-2}, and $t_{\rm off} = t_{\rm on} = 2$ ps and $t_{\rm p} = 20$ ps. The dashed curve represents the scaled $\varepsilon^2(t)$, see Eqs. (4) and (B2). The horizontal line is set at $\langle \mu_Z \rangle = 0$.

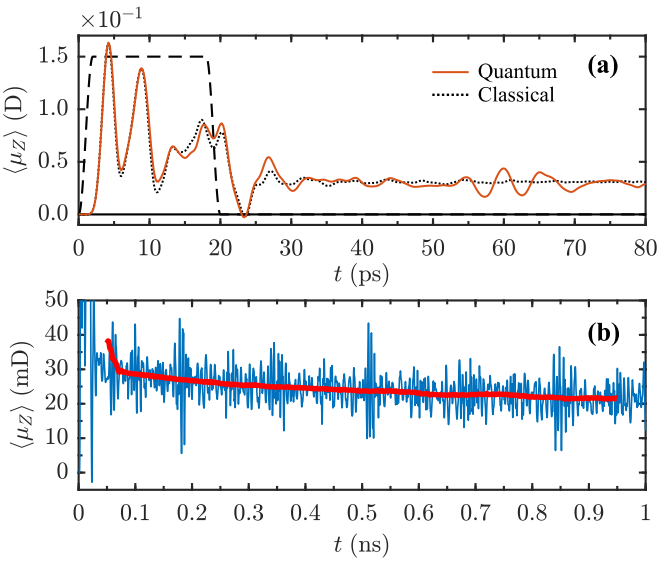

FIG. 6. Quantum expectation value of the projection of the molecular dipole on the Z axis, $\langle \mu_Z \rangle (t)$, for the case of a ($R$)-PPO molecule excited by the optical centrifuge pulse. Parameters are similar to those of Fig. 5. (a) The short-time dipole signal (solid) and its classical counterpart (dotted). The dashed curve represents the scaled $\varepsilon^2(t)$, see Eqs. (4) and (B2). (b) Blue (gray) indicates long-time dynamics and red (black) the 100-ps time average, $\overline{\langle \mu_Z \rangle (t)} = (\Delta t)^{-1} \int_{t-\Delta t/2}^{t+\Delta t/2} \langle \mu_Z \rangle (t') dt'$.

a function of time, $\langle \mu_Z \rangle (t)$ resulting from excitation by the optical centrifuge. The temperature changes in steps of 10 K in the range of $T \in [10, 150]$ K.

Akin to the double-pulse scheme, excitation by the optical centrifuge results in enantioselective dipole signal. The signal drops down when the centrifuge is switched off after 20 ps. However, the orientation signal does not vanish completely but levels off at a nonzero value. Although the amplitude of the transient signal is higher in the case of the double-pulse excitation, the amplitudes of the long-time signals are higher in this scenario, making the optical centrifuge more efficient in inducing the permanent dipole orientation. The amplitudes of the signals, both during the driven and field-free dynamics periods, are temperature dependent and decrease with temperature.

To investigate the long-lasting dynamics of the induced dipole moment, we carried out a fully quantum-mechanical simulation of the centrifuge-driven (R)-PPO rotational dynamics. The centrifuge pulse had the same parameters as shown in the caption to Fig. 5, while the rotational temperature was set to $T = 5$ K. Such a pulse excites angular momenta of up to $40\hbar$, with the mean excitation of about $30\hbar$, which is higher as compared to the previous double-pulse excitation example and significantly above the average thermal value of $3.5\hbar$. Higher angular momentum results in a better quantum-classical agreement as compared to the double-pulse excitation. The short-time dipole signal is shown in Fig. 6(a). During the pulse, the polarization peaks at about 0.15 D, and it stays practically constant at the level of ≈0.03 D after the end of the pulse, with a small-amplitude beating structure present at long times. For comparison, the classical signal obtained under the same conditions is plotted and the correspondence with the quantum results is very good up to $t \approx 60$ ps. On the nanosecond timescale [Fig. 6(b)], one can observe multiple beats; however, the coarse-grained time-averaged quantum signal remains positive and almost as constant as the classically predicted one.

Dynamical tunneling. Due to the coupling of different K states by the rotational Hamiltonian [see Eq. (B3)], the quantum-mechanical rigid asymmetric top does not have eigenstates with the angular momentum being oriented within the molecular frame. As a consequence, any state that is internally oriented at some point in time cannot be an eigenstate and will oscillate between being oriented and antioriented, an effect known as dynamical tunneling [53]. In other words, a clockwise internal rotation would eventually become counterclockwise, and vice versa. This leads to a breakdown of quantum-classical analogy, as the classical model introduced in Sec. II assumes a strict separation of clockwise and counterclockwise rotation (no interchange between T_k^+ and T_k^-). Therefore, one would expect no permanent orientation after turn-off of all external fields for a quantum-mechanical chiral rotor.

Yet, in spite of the dynamical tunneling, our simulations show a significant long-time orientation of the quantum rotors, equal in magnitude to the classical model. The reason is that the dynamical tunneling time grows very fast with the angular momentum [54], being larger the more the angular momentum is (anti-)oriented along the a or c axis. Indeed, already for $J = 10\hbar$, the tunneling time may exceed microseconds [54], explaining why orientation was observed in the quantum simulations on a nanosecond timescale. As a matter of fact, the slight decrease of the baseline visible in Fig. 6(b) (thick red line) is possibly a signature of the dynamical tunneling.

At this point one should also note that while dynamical tunneling would be of greater importance on longer timescales than those presented here, other effects (neglected here), like rovibrational couplings, hyperfine structure [55], and intermolecular collisions, are likely of higher importance and would probably bury any signs of the dynamical tunneling in an actual experiment.

Extrapolation to room temperature. Due to the statistical nature of our classical simulations on one hand and basis

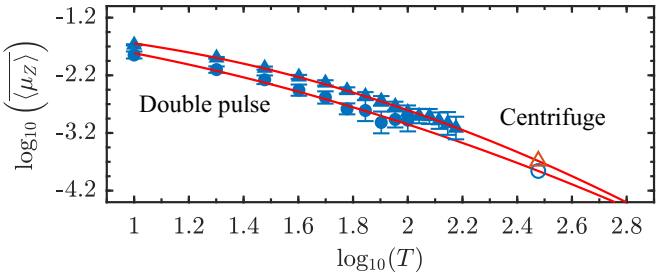

FIG. 7. Logarithmic scale plot of the average constant component of $\langle\mu_Z\rangle$, $\overline{\langle\mu_Z\rangle} = (t_{\max}-\tau)^{-1}\int_{\tau}^{t_{\max}}\langle\mu_Z\rangle(t')dt'$ as a function of temperature. For the double-pulse excitation (circles) $\tau = 12$ ps, while for the centrifuge (triangles) $\tau = 30$ ps (see Figs. 3 and 5). The error bars are obtained using the standard error propagation formula [56]. Solid lines are fit functions of the form $f(x) = ax^2 + bx + c$. The parameter triplets (a, b, c) are $(-0.47, 0.24, -1.42)$ and $(-0.31, -0.30, -1.20)$ for the centrifuge and the double pulse, respectively. The large open triangle and circle correspond to temperature $T = 300$ K, and their coordinates are (2.48,−3.69) and (2.48,−3.86) for the centrifuge and double pulse, respectively.

size limitations of the quantum simulation on the other, direct simulations at room temperature are highly numerically demanding; therefore we resort to extrapolation. Figure 7 shows the average long-term value of the classically calculated $\langle\mu_Z\rangle$, denoted by $\overline{\langle\mu_Z\rangle}$ as a function of temperature on the double logarithmic scale. The error bars for $\log_{10}(\overline{\langle\mu_Z\rangle})$ are obtained by the standard error propagation formula [56] based on the variance of $\langle\mu_Z\rangle$. The points are fit by a polynomial, and each point is assigned a weight equal to the inverse of its variance. The fit allows one to extrapolate the results to temperatures beyond those simulated. The predicted value of the permanent dipole at room temperature is $\approx 1.3\times10^{-4}$ D and $\approx 2.0\times10^{-4}$ D for the double-pulse and centrifuge excitation schemes, respectively (see Fig. 7). Because of the relatively high vapor pressure of propylene oxide at room temperature [57], even such modest values of the mean molecular dipole moment result in a sizable macroscopic polarization in the gas sample and cause a collective electric field of about 0.05 V/m in the focal region of a laser beam focused to a spot of $r_0 \sim 10$ μm and having the Rayleigh range of about $z_R \sim 1$ mm. The magnitude and longevity of this field (and the corresponding light-induced voltage) favor its detection using high-speed nanosecond electronics.

The appearance of long-time orientation in a gas sample can be detected by means of Coulomb explosion [9,10,16,20,21,46] and nonlinear optics through high harmonic generation of various orders [58–61], especially by means of the second harmonic generation. Another approach to detecting the induced orientation is by measuring terahertz emission due to free induction decay of coherently oscillating molecular dipoles [62–64].

IV. CONCLUSIONS

Summarizing, we have demonstrated long-lived orientation of chiral molecules by laser fields with twisted polarization using both classical mechanics and fully quantum-mechanical treatments. The problem was analyzed using propylene oxide molecules, as an example, and considering two different implementations of the twisted optical field: (i) a pair of delayed cross-polarized laser pulses and (ii) an optical centrifuge. We found very good agreement between the classical and quantum approaches over a wide range of experimentally relevant parameters and over an extended time range. The phenomenon of persistent orientation of chiral molecules was conjectured in our previous papers [27,28] utilizing a classical approach, but its validity is now verified on a much longer timescale (several orders of magnitude longer) where the use of quantum treatment is unavoidable. The sign of the oriented dipole moment depends on both the sense of polarization twisting and the handedness of the molecule. This long-lasting orientation provides modalities for detecting molecular chirality with the help of optical harmonics generation, or direct high-speed measurements of electric fields caused by laser-induced macroscopic polarization of the gas. Moreover, it is well known that optical preorientation of molecules affects their deflection by inhomogeneous fields (see, e.g. [65–67], references therein, and recent reviews [68–70]). Enantioselective orientation effects considered in this paper may open up new avenues for separation of molecular enantiomers.

We note that ongoing experiments in Milner' s group show initial signals of the long-time enantioselective orientation, supporting our theoretical predictions. A report on these results and the corresponding theoretical analysis will be published elsewhere [71].

ACKNOWLEDGMENTS

The authors appreciate useful discussions with A. A. Milner and V. Milner. This work was supported by the Israel Science Foundation (Grant No. 746/15), the ISF-NSFC joint research program (Grant No. 2520/17), and by a grant to P.B. by the Natural Sciences and Engineering Research Council of Canada. I.A. acknowledges support as the Patricia Elman Bildner Professorial Chair and thanks the UBC Department of Physics & Astronomy for hospitality extended to him during his sabbatical stay while part of this work was being done. This research was made possible in part by the historic generosity of the Harold Perlman Family.

I.T. and J.F. contributed equally to this work.

APPENDIX A: DERIVATION OF EQ. (1)

As discussed in the main text, we consider an excitation by a pair of delayed cross-polarized laser pulses. The first pulse is polarized along the laboratory X axis, while the polarization of the second one is in the XY plane at $+\pi/4$ to the X axis. We assume that the first pulse induces a perfect alignment of the most polarizable molecular axis (x_1) along the X axis. Initially, we consider only half of all molecules, in which the most polarizable axis points along $+X$ [see Fig. 2(a)]. Angle $\varphi \in [0, 2\pi)$ is the angle between the Y axis and the x_2 axis, lying in the YZ plane [see Fig. 2(b)]. The aligned molecules are uniformly distributed in φ. The interaction potential U and torque $\mathbf{T}$ induced by a nonresonant optical field are given by

$$U = -\tfrac{1}{2}\langle \mathbf{d}_{\rm ind}\cdot\mathbf{E}\rangle, \quad \mathbf{T} = \langle \mathbf{d}_{\rm ind}\times\mathbf{E}\rangle, \tag{A1}$$

where the angle brackets denote time averaging over the optical cycle, $\mathbf{d}_{\rm ind} = \boldsymbol{\alpha}\mathbf{E}$ is the induced dipole, $\boldsymbol{\alpha}$ is the

polarizability tensor, and $\mathbf{E}$ is the vector of the electric field. The interaction with a permanent molecular dipole vanishes, because the optical fields (having typical frequency 10^{14} Hz) considered in this work are far detuned from any dipole transitions (having typical frequency 10^{11} Hz). The duration of the laser pulses is assumed to be short as compared to the typical rotation periods of the chiral molecules; therefore the effect of the second pulse is considered in the impulsive approximation, $\Delta\mathbf{L} \propto \mathbf{T}$.

The second pulse (twisted with respect to the first one) induces unidirectional rotation in the XY plane, resulting in orientation of $\langle \boldsymbol{\ell} \rangle$ along Z, which constitutes the first criterion for the long-lasting orientation. In addition, there is an orienting torque acting on the aligned most polarizable axis, x_1. To check whether the second criterion for the long-lasting orientation is satisfied, we evaluate the torques along the molecular a and c axes. For this, we begin with transforming the electric field coordinates from the laboratory frame of reference to the frame of polarizability tensor principal axes

$$\mathbf{E}_\alpha \propto R_X(-\varphi)(1,1,0)^T, \tag{A2}$$

where $\mathbf{E}_\alpha$ denotes the column vector of electric field coordinates in the frame of polarizability tensor principal axes, $(1,1,0)^T$ represents the second pulse lying in the XY plane at the $+\pi/4$ angle, and $R_X(\theta)$ is the canonical rotation matrix. We evaluate the torque, using

$$\mathbf{T}_\alpha \propto \left[\begin{pmatrix} \alpha_{11} & 0 & 0 \\ 0 & \alpha_{22} & 0 \\ 0 & 0 & \alpha_{33} \end{pmatrix} \mathbf{E}_\alpha \right] \times \mathbf{E}_\alpha. \tag{A3}$$

The torque is transformed to the frame of inertia tensor principal axes by an orthogonal matrix R, defined by $\mathbf{v}_I = R\mathbf{v}_\alpha$, where $\mathbf{v}_I$ denotes the column vector of coordinates of some vector $\vec{v}$ in the frame of inertia tensor principal axes. In the frame of principal axes of inertia tensor the torque is given by

$$\mathbf{T}_I \equiv (\tau_a, \tau_b, \tau_c)^T \propto R\mathbf{T}_\alpha. \tag{A4}$$

Since the molecule is chiral, polarizability tensor principal axes and inertia tensor principal axes frames do not align [see Fig. 1(a) in the main text] and R is not diagonal,

$$R = \begin{pmatrix} \mathbf{a}\cdot\mathbf{x}_1 & \mathbf{a}\cdot\mathbf{x}_2 & \mathbf{a}\cdot\mathbf{x}_3 \\ \mathbf{b}\cdot\mathbf{x}_1 & \mathbf{b}\cdot\mathbf{x}_2 & \mathbf{b}\cdot\mathbf{x}_3 \\ \mathbf{c}\cdot\mathbf{x}_1 & \mathbf{c}\cdot\mathbf{x}_2 & \mathbf{c}\cdot\mathbf{x}_3 \end{pmatrix}, \tag{A5}$$

where bold letters denote the unit vectors along the corresponding axes. The explicit expression for τ_k $(k = a, c)$ is given by Eq. (1) (in the main text) $\tau_k \propto C_k \sin(2\varphi) + D_k \sin(\varphi + \phi_k)$, where $C_k = (\alpha_{33} - \alpha_{22})R_{k1}/2$, $D_k = \sqrt{A_k^2 + B_k^2}$, $A_k = (\alpha_{11} - \alpha_{33})R_{k2}$, $B_k = (\alpha_{11} - \alpha_{22})R_{k3}$, and $\tan(\phi_k) = B_k/A_k$. When the off-diagonal elements of R differ from zero, the subdomains of positive and negative τ_k in the interval $\varphi \in [0, 2\pi)$ are not equal, which is precisely the required T_k^+ vs T_k^- asymmetry. When the two frames do coincide (nonchiral molecule), R becomes diagonal, resulting in torques $\tau_a = C_a \sin(2\varphi)$ and $\tau_c = A_c \sin(\varphi)$. In this case, the T_k^+ vs T_k^- symmetry is preserved. For the complimentary enantiomer [(*S*)-PPO], signs of some of the elements of R_{nm} are reversed, resulting in the opposite orientation direction. As the two enantiomers are related by the reflection transformation, we can choose, without loss of generality, the x_1x_2 plane as the plane of reflection. As a result, signs of all projections on the x_3 axis change sign,

$$R = \begin{pmatrix} \mathbf{a}\cdot\mathbf{x}_1 & \mathbf{a}\cdot\mathbf{x}_2 & -\mathbf{a}\cdot\mathbf{x}_3 \\ \mathbf{b}\cdot\mathbf{x}_1 & \mathbf{b}\cdot\mathbf{x}_2 & -\mathbf{b}\cdot\mathbf{x}_3 \\ \mathbf{c}\cdot\mathbf{x}_1 & \mathbf{c}\cdot\mathbf{x}_2 & -\mathbf{c}\cdot\mathbf{x}_3 \end{pmatrix}, \tag{A6}$$

leading to the change of ϕ_k sign in Eq. (3). The opposite sign of ϕ_k leads to exchange of positive and negative subdomains of $\tau_k(\varphi)$ in the interval $\varphi \in [0, 2\pi)$. This is interpreted as a change of orientation direction.

APPENDIX B: QUANTUM-MECHANICAL SIMULATION

For our quantum-mechanical simulations of the laser-driven dynamics of the chiral molecules, we used the following expressions for the envelopes of the short pulses:

$$\varepsilon^2(t)/\mathcal{E}_0^2 = \begin{cases} \cos^2\left(\frac{\pi}{2}\frac{t-t_0}{\tau_0}\right) & |t - t_0| \leqslant \tau_0 \\ 0 & \text{otherwise,} \end{cases} \tag{B1}$$

where τ_0 is the FWHM of the intensity profile and the optical centrifuge

$$\varepsilon^2(t)/\mathcal{E}_0^2 = \begin{cases} \sin^2\left(\frac{\pi t}{2\tau_{\text{on}}}\right) & 0 \leqslant t < t_{\text{on}} \\ 1 & t_{\text{on}} \leqslant t < t_{\text{p}} - t_{\text{off}} \\ \sin^2\left[\frac{\pi(t-t_{\text{p}})}{2\tau_{\text{off}}}\right] & t_{\text{p}} - t_{\text{off}} \leqslant t < t_{\text{p}} \\ 0 & t_{\text{p}} \leqslant t. \end{cases} \tag{B2}$$

The first step in our numerical scheme is to express the Hamiltonian in the basis of symmetric-top wave functions $|JKM\rangle$. Here, the quantum number J is the total angular momentum, K is its projection onto the molecule-fixed c axis, and M is its projection onto the space-fixed Z axis. The nonzero matrix elements of the asymmetric-top rotational Hamiltonian are given by [51]

$$\begin{aligned} \langle JKM|H_{\text{rot}}|JKM\rangle &= \frac{C+A}{2}[J(J+1) - K^2] + BK^2 \\ \langle JKM|H_{\text{rot}}|JK \pm 2M\rangle &= \frac{C-A}{4} f(J, K \pm 1), \end{aligned} \tag{B3}$$

where

$$f(J,K) = \sqrt{(J^2 - K^2)[(J+1)^2 - K^2]}, \tag{B4}$$

and $A = \hbar^2/(2I_a)$, $B = \hbar^2/(2I_b)$, and $C = \hbar^2/(2I_c)$ are the rotational constants. Note that H_{rot} couples only levels with different K's; therefore the asymmetric-top eigenfunctions can be expressed as $|J\tau M\rangle = \sum_K c_K^{(J,\tau,M)} |JKM\rangle$, where τ enumerates the "asymmetric-top" levels [51]. The coefficients $c_K^{(J,\tau,M)}$ are determined by numerically diagonalizing H_{rot}. Note that the eigenenergies $E_{J,\tau}$ are degenerate in the quantum number M. The interaction potentials with the laser fields is given by $V = -\langle \mathbf{E}\cdot\mathbf{d}_{\text{ind}} \rangle/2 = -\langle \mathbf{E}\cdot(\boldsymbol{\alpha}\mathbf{E}) \rangle/2$, where the angle brackets denote time averaging over the optical cycle, $\mathbf{d}_{\text{ind}} = \boldsymbol{\alpha}\mathbf{E}$ is the induced dipole, $\boldsymbol{\alpha}$ is the polarizability tensor, and $\mathbf{E}$ is the vector of the electric field. It is beneficial to work in a spherical basis [51,72], in which case the transformation law for vectors and tensors has a simple form:

$$T_p^{(r)} = \sum_q D_{p,q}^{(r)*} T_q^{(r)}, \tag{B5}$$

where $T_p^{(r)}$ is a spherical tensor of rank r, and the indices p and q are associated with the laboratory- and molecule-fixed frames, respectively. $D_{p,q}^{(r)*}(\Omega)$ is the conjugate of the Wigner D matrix, and Ω denotes the set of three Euler angles. Note that for convenience, we suppress the angle dependence of the Wigner D matrices. In a spherical basis, the double contraction required in the evaluation of the potential is given by [72]

$$V = -\frac{1}{2}\sum_{r=0}^{2}\sum_{k=-r}^{r}(-1)^k \left\langle A_{\mathrm{lab},k}^{(r)}\right\rangle \alpha_{\mathrm{lab},-k}^{(r)}. \tag{B6}$$

We chose to evaluate the potential in the laboratory-fixed frame. Here the angle brackets denote averaging over the optical cycle, $\alpha_{\mathrm{lab},-k}^{(r)}$ are the spherical tensor elements of molecular polarizability in the laboratory frame, and $A_{\mathrm{lab},k}^{(r)}$ is the same for the electric field vector. Using the spherical basis, we evaluate the potential in the laboratory-fixed frame. $A_{\mathrm{lab},k}^{(r)}$'s are given by

$$\begin{aligned}
A_{\mathrm{lab},0}^{(0)} &= -\frac{1}{\sqrt{3}}\mathbf{E}\cdot\mathbf{E}\\
A_{\mathrm{lab},0}^{(2)} &= \frac{1}{\sqrt{6}}\left(3E_Z^2 - \mathbf{E}\cdot\mathbf{E}\right)\\
A_{\mathrm{lab},\pm1}^{(2)} &= \mp E_X E_Z - iE_Y E_Z\\
A_{\mathrm{lab},\pm2}^{(2)} &= \frac{1}{2}\left(E_X^2 - E_Y^2 \pm i2E_X E_Y\right),
\end{aligned} \tag{B7}$$

while the polarizability requires transformation from the molecular to the laboratory frame, $\alpha_{\mathrm{lab},p}^{(r)} = \sum_q D_{p,q}^{(r)*}\alpha_{\mathrm{mol},q}^{(r)}$, and

$$\begin{aligned}
\alpha_{\mathrm{mol},0}^{(0)} &= -\frac{1}{\sqrt{3}}(\alpha_{aa}+\alpha_{bb}+\alpha_{cc})\\
\alpha_{\mathrm{mol},0}^{(2)} &= \frac{1}{\sqrt{6}}(2\alpha_{cc}-\alpha_{aa}-\alpha_{bb})\\
\alpha_{\mathrm{mol},\pm1}^{(2)} &= \mp\alpha_{ac} - i\alpha_{bc}\\
\alpha_{\mathrm{mol},\pm2}^{(2)} &= \frac{1}{2}(\alpha_{aa}-\alpha_{bb} \pm 2i\alpha_{ab}).
\end{aligned} \tag{B8}$$

α_{ij}'s are the Cartesian components of the polarizability tensor in the frame of inertia tensor principal axes (see Table I). The potential is given by [26]

$$\begin{aligned}
V = -\frac{|\varepsilon(t)|^2}{4}\Bigg[&-\frac{1}{\sqrt{3}}\alpha_{\mathrm{mol},0}^{(0)}D_{0,0}^{(0)*} - \frac{1}{\sqrt{6}}D_{0,k}^{(2)*}\alpha_{\mathrm{mol},k}^{(2)}\\
&+\frac{\alpha_{\mathrm{mol},k}^{(2)}}{2}\left(e^{i2\gamma}D_{-2,k}^{(2)*} + e^{-i2\gamma}D_{2,k}^{(2)*}\right)\Bigg],
\end{aligned} \tag{B9}$$

where summation over the repeated index $k=-2,\ldots,2$ is implied. The time averaging over the optical cycle adds an overall factor of 1/2 (included). The field envelope $\varepsilon(t)$ appearing in the above is defined by Eqs. (B1) and (B2). The expression is valid for laser fields polarized in the XY plane, with γ being the angle between the instantaneous polarization axis and the X axis. In the double-pulse scheme, the angle $\gamma=\pi/4$, while in the case of the optical centrifuge the angle is time dependent $\gamma=\beta t^2$. To calculate the couplings $\langle JKM|V|J'K'M'\rangle$, we use the relation [51]

$$\begin{aligned}
&\langle JKM|D_{p,q}^{(s)*}|J'K'M'\rangle\\
&\quad= (-1)^{M-K}\sqrt{(2J+1)(2J'+1)}\\
&\qquad\times\begin{pmatrix} J & s & J'\\ -M & p & M'\end{pmatrix}\begin{pmatrix} J & s & J'\\ -K & q & K'\end{pmatrix},
\end{aligned} \tag{B10}$$

where the large brackets denote Wigner 3-j symbols.

To calculate the dynamics during the laser pulse, we solve the time-dependent Schrödinger equation. In particular, the rotational wave function is expressed as a linear combination of the symmetric top wave functions, $|\Psi(t)\rangle = \sum_{JKM} c_{JKM}(t)\,|JKM\rangle$, and the resulting set of coupled differential equations for the coefficients $c_{JKM}(t)$ is solved by numerical integration. To calculate the dynamics in the absence of a laser pulse, we express the wave function in the eigenbasis of H_{rot} [see Eq. (B3)] in which the field-free time evolution is simply given as

$$\Psi(t+\Delta t) = \sum_{J,\tau,M} c_{J\tau M}e^{-iE_{J,\tau}t/\hbar}\,|J,\tau,M\rangle\,, \tag{B11}$$

with

$$c_{J\tau M} = \sum_K c_K^{(J,\tau,M)*}c_{JKM}. \tag{B12}$$

The polarization is given as the expectation value

$$P(t) \equiv \langle \boldsymbol{\mu}\cdot\hat{\mathbf{Z}}\rangle\,(t) = \langle\Psi(t)|D_{0,q}^{(1)*}\mu_{\mathrm{mol},q}^{(1)}|\Psi(t)\rangle\,, \tag{B13}$$

where summation over the repeated index $q=-1,0,1$ is implied. The spherical tensor components of the molecular dipole are given in terms of components of the dipole expressed in the Cartesian frame of inertia tensor principal axes $\mu_{\mathrm{mol},\pm1}^{(1)} = (\mp\mu_a - i\mu_b)/\sqrt{2}$ and $\mu_{\mathrm{mol},0}^{(1)} = \mu_c$.

The alignment of the most polarizable axis $\mathbf{m}$ towards the X axis is given by the expectation value $O(t) \equiv \langle(\mathbf{m}(t)\cdot\hat{\mathbf{X}})^2\rangle$. To use the spherical basis formulas introduced above, we rewrite the alignment factor in a double-contraction format (like the potential) $(\mathbf{m}\cdot\hat{\mathbf{X}})^2 = \mathbf{m}\cdot(\boldsymbol{\chi}\mathbf{m})$, where $\boldsymbol{\chi}$ is an operator that extracts the X component of the vector $\mathbf{m}$. Now, we can use $(\mathbf{m}\cdot\hat{\mathbf{X}})^2 = \sum_{r=0}^{2}\sum_{k=-r}^{r}(-1)^k A_{\mathrm{mol},k}^{(r)}\chi_{\mathrm{mol},-k}^{(r)}$. The Cartesian representation of $\boldsymbol{\chi}$ in the laboratory-fixed frame is given by the matrix

$$\chi_{\mathrm{lab}} = \begin{pmatrix} 1 & 0 & 0\\ 0 & 0 & 0\\ 0 & 0 & 0\end{pmatrix}, \tag{B14}$$

and therefore its components in the spherical basis are

$$\begin{aligned}
\chi_{\mathrm{lab},0}^{(0)} &= -\frac{1}{\sqrt{3}}(\chi_{XX}+\chi_{YY}+\chi_{ZZ}) = -\frac{1}{\sqrt{3}}\\
\chi_{\mathrm{lab},0}^{(2)} &= \frac{1}{\sqrt{6}}(2\chi_{ZZ}-\chi_{XX}-\chi_{YY}) = -\frac{1}{\sqrt{6}}\\
\chi_{\mathrm{lab},\pm1}^{(2)} &= \mp\chi_{XZ} - i\chi_{YZ} = 0\\
\chi_{\mathrm{lab},\pm2}^{(2)} &= \frac{1}{2}(\chi_{XX}-\chi_{YY} \pm 2i\chi_{XY}) = \frac{1}{2},
\end{aligned} \tag{B15}$$

and in the molecular frame

$$\chi^{(r)}_{\mathrm{mol},q} = \sum_p D^{(r)}_{p,q}\chi^{(r)}_{\mathrm{lab},p} = \sum_p (-1)^{p-q} D^{(r)*}_{-p,-q}\chi^{(r)}_{\mathrm{lab},p}. \tag{B16}$$

In addition,

$$\begin{aligned} A^{(0)}_{\mathrm{mol},0} &= -\frac{1}{\sqrt{3}}\left(m_a^2 + m_b^2 + m_c^2\right) \\ A^{(2)}_{\mathrm{mol},0} &= \frac{1}{\sqrt{6}}\left(2m_c^2 - m_a^2 - m_b^2\right) \\ A^{(2)}_{\mathrm{mol},\pm1} &= \mp m_a m_c - i m_b m_c \\ A^{(2)}_{\mathrm{mol},\pm2} &= \frac{1}{2}\left(m_a^2 - m_b^2 \pm 2i m_a m_b\right). \end{aligned} \tag{B17}$$

Finally, the alignment factor is given by

$$\begin{aligned} O(t) = {} & A^{(0)}_{\mathrm{mol},0} D^{(0)}_{00} \chi^{(0)}_{\mathrm{lab},0} + A^{(2)}_{\mathrm{mol},-2} D^{(2)}_{p,2} \chi^{(2)}_{\mathrm{lab},p} \\ & - A^{(2)}_{\mathrm{mol},-1} D^{(2)}_{p,1} \chi^{(2)}_{\mathrm{lab},p} + A^{(2)}_{\mathrm{mol},0} D^{(2)}_{p,0} \chi^{(2)}_{\mathrm{lab},p} \\ & - A^{(2)}_{\mathrm{mol},1} D^{(2)}_{p,-1} \chi^{(2)}_{\mathrm{lab},p} + A^{(2)}_{\mathrm{mol},2} D^{(2)}_{p,-2} \chi^{(2)}_{\mathrm{lab},p}, \end{aligned} \tag{B18}$$

where summation over the repeated index $p = -2, \ldots, 2$ is implied. The matrix elements of these expectation values are calculated using Eq. (B10). To include thermal effects, we do ensemble averaging: The initial wave function is set to an eigenstate, $|\Psi(t=0)\rangle = |J\tau M\rangle$, and the expectation values are calculated for this initial state as $P_{J,\tau,M}(t)$ and $O_{J,\tau,M}(t)$. The final expectation value is then the thermally averaged sum

$$P(t) = \sum_{J,\tau,M} P_{J,\tau,M}(t) Z^{-1} \exp\left[-\frac{E_{J,\tau}}{k_B T}\right], \tag{B19}$$

$$O(t) = \sum_{J,\tau,M} O_{J,\tau,M}(t) Z^{-1} \exp\left[-\frac{E_{J,\tau}}{k_B T}\right], \tag{B20}$$

where k_B is the Boltzmann constant, T the temperature, and $Z = \sum_{J,\tau,M} \exp[-E_{J,\tau}/k_B T]$ is the canonical partition function. To keep the calculation numerically feasible, only initial states with an angular momentum of $J \leqslant 10$ were included in the ensemble; the expectation values were found to have converged at this value for temperatures of at least $T = 5$ K.

[1] F. A. Cotton, *Chemical Applications of Group Theory*, 3rd ed. (John Wiley & Sons, Hoboken, NJ, 1990).

[2] G. H. Wagnière, *On Chirality and the Universal Asymmetry: Reflections on Image and Mirror Image* (Wiley-VCH, Weinheim, 2007).

[3] M. Shapiro and P. Brumer, *Quantum Control of Molecular Processes*, 2nd ed. (Wiley-VCH, Weinheim, 2012).

[4] P. Král and M. Shapiro, Cyclic Population Transfer in Quantum Systems with Broken Symmetry, Phys. Rev. Lett. **87**, 183002 (2001).

[5] P. Brumer, E. Frishman, and M. Shapiro, Principles of electric-dipole-allowed optical control of molecular chirality, Phys. Rev. A **65**, 015401 (2001).

[6] Y. Li, C. Bruder, and C. P. Sun, Generalized Stern-Gerlach Effect for Chiral Molecules, Phys. Rev. Lett. **99**, 130403 (2007).

[7] C. Lux, M. Wollenhaupt, T. Bolze, Q. Liang, J. Köhler, C. Sarpe, and T. Baumert, Circular dichroism in the photoelectron angular distributions of camphor and fenchone from multiphoton ionization with femtosecond laser pulses, Angew. Chem. **51**, 5001 (2012).

[8] D. Patterson, M. Schnell, and J. M. Doyle, Enantiomer-specific detection of chiral molecules via microwave spectroscopy, Nature (London) **497**, 475 (2013).

[9] M. Pitzer, M. Kunitski, A. S. Johnson, T. Jahnke, H. Sann, F. Sturm, L. Ph. H. Schmidt, H. Schmidt-Böcking, R. Dörner, J. Stohner, J. Kiedrowski, M. Reggelin, S. Marquardt, A. Schießer, R. Berger, and M. S. Schöffler, Direct determination of absolute molecular stereochemistry in gas phase by Coulomb explosion imaging, Science **341**, 1096 (2013).

[10] P. Herwig, K. Zawatzky, M. Grieser, O. Heber, B. Jordon-Thaden, C. Krantz, O. Novotný, R. Repnow, V. Schurig, D. Schwalm, Z. Vager, A. Wolf, O. Trapp, and H. Kreckel, Imaging the absolute configuration of a chiral epoxide in the gas phase, Science **342**, 1084 (2013).

[11] C. S. Lehmann, N. B. Ram, I. Powis, and M. H. M. Janssen, Imaging photoelectron circular dichroism of chiral molecules by femtosecond multiphoton coincidence detection, J. Chem. Phys. **139**, 234307 (2013).

[12] M. H. M. Janssen and I. Powis, Detecting chirality in molecules by imaging photoelectron circular dichroism, Phys. Chem. Chem. Phys. **16**, 856 (2014).

[13] D. Patterson and M. Schnell, New studies on molecular chirality in the gas phase: Enantiomer differentiation and determination of enantiomeric excess, Phys. Chem. Chem. Phys. **16**, 11114 (2014).

[14] A. Steinbacher, P. Nuernberger, and T. Brixner, Optical discrimination of racemic from achiral solutions, Phys. Chem. Chem. Phys. **17**, 6340 (2015).

[15] C. Lux, A. Senftleben, C. Sarpe, M. Wollenhaupt, and T. Baumert, Photoelectron circular dichroism observed in the above-threshold ionization signal from chiral molecules with femtosecond laser pulses, J. Phys. B **49**, 02LT01 (2015).

[16] L. Christensen, J. H. Nielsen, C. S. Slater, A. Lauer, M. Brouard, and H. Stapelfeldt, Using laser-induced Coulomb explosion of aligned chiral molecules to determine their absolute configuration, Phys. Rev. A **92**, 033411 (2015).

[17] A. Kastner, C. Lux, T. Ring, S. Züllighoven, C. Sarpe, A. Senftleben, and T. Baumert, Enantiomeric excess sensitivity to below one percent by using femtosecond photoelectron circular dichroism, Chem. Phys. Chem. **17**, 1119 (2016).

[18] S. Eibenberger, J. Doyle, and D. Patterson, Enantiomer-Specific State Transfer of Chiral Molecules, Phys. Rev. Lett. **118**, 123002 (2017).

[19] S. Beaulieu, A. Comby, D. Descamps, B. Fabre, G. A. Garcia, R. Géneaux, A. G. Harvey, F. Légaré, Z. Mašín, L. Nahon, A. F. Ordonez, S. Petit, B. Pons, Y. Mairesse, O. Smirnova, and V. Blanchet, Photoexcitation circular dichroism in chiral molecules, Nat. Phys. **14**, 484 (2018).

[20] M. Pitzer, R. Berger, J. Stohner, R. Dörner, and M. Schöffler, Investigating absolute stereochemical configuration with Coulomb explosion imaging, Chimia **72**, 384 (2018).

[21] K. Fehre, S. Eckart, M. Kunitski, M. Pitzer, S. Zeller, C. Janke, D. Trabert, J. Rist, M. Weller, A. Hartung, L. Ph. H. Schmidt, T. Jahnke, R. Berger, R. Dörner, and M. S. Schöffler, Enantioselective fragmentation of an achiral molecule in a strong laser field, Sci. Adv. **5**, eaau7923 (2019).

[22] O. Neufeld, D. Ayuso, P. Decleva, M. Y. Ivanov, O. Smirnova, and O. Cohen, Ultrasensitive Chiral Spectroscopy by Dynamical Symmetry Breaking in High Harmonic Generation, Phys. Rev. X **9**, 031002 (2019).

[23] S. Rozen, A. Comby, E. Bloch, S. Beauvarlet, D. Descamps, B. Fabre, S. Petit, V. Blanchet, B. Pons, N. Dudovich, and Y. Mairesse, Controlling Subcycle Optical Chirality in the Photoionization of Chiral Molecules, Phys. Rev. X **9**, 031004 (2019).

[24] M. Leibscher, T. F. Giesen, and C. P. Koch, Principles of enantio-selective excitation in three-wave mixing spectroscopy of chiral molecules, J. Chem. Phys. **151**, 014302 (2019).

[25] M. Shapiro, E. Frishman, and P. Brumer, Coherently Controlled Asymmetric Synthesis with Achiral Light, Phys. Rev. Lett. **84**, 1669 (2000).

[26] A. Yachmenev and S. N. Yurchenko, Detecting Chirality in Molecules by Linearly Polarized Laser Fields, Phys. Rev. Lett. **117**, 033001 (2016).

[27] E. Gershnabel and I. Sh. Averbukh, Orienting Asymmetric Molecules by Laser Fields with Twisted Polarization, Phys. Rev. Lett. **120**, 083204 (2018).

[28] I. Tutunnikov, E. Gershnabel, S. Gold, and I. Sh. Averbukh, Selective orientation of chiral molecules by laser fields with twisted polarization, J. Phys. Chem. Lett. **9**, 1105 (2018).

[29] S. Fleischer, Y. Khodorkovsky, Y. Prior, and I. Sh. Averbukh, Controlling the sense of molecular rotation, New J. Phys. **11**, 105039 (2009).

[30] K. Kitano, H. Hasegawa, and Y. Ohshima, Ultrafast Angular Momentum Orientation by Linearly Polarized Laser Fields, Phys. Rev. Lett. **103**, 223002 (2009).

[31] Y. Khodorkovsky, K. Kitano, H. Hasegawa, Y. Ohshima, and I. Sh. Averbukh, Controlling the sense of molecular rotation: Classical versus quantum analysis, Phys. Rev. A **83**, 023423 (2011).

[32] O. Korech, U. Steinitz, R. J. Gordon, I. Sh. Averbukh, and Y. Prior, Observing molecular spinning via the rotational Doppler effect, Nat. Photonics **7**, 711 (2013).

[33] K. Mizuse, K. Kitano, H. Hasegawa, and Y. Ohshima, Quantum unidirectional rotation directly imaged with molecules, Sci. Adv. **1**, e1400185 (2015).

[34] K. Lin, Q. Song, X. Gong, Q. Ji, H. Pan, J. Ding, H. Zeng, and J. Wu, Visualizing molecular unidirectional rotation, Phys. Rev. A **92**, 013410 (2015).

[35] S. Zhdanovich, A. A. Milner, C. Bloomquist, J. Floß, I. Sh. Averbukh, J. W. Hepburn, and V. Milner, Control of Molecular Rotation with a Chiral Train of Ultrashort Pulses, Phys. Rev. Lett. **107**, 243004 (2011).

[36] C. Bloomquist, S. Zhdanovich, A. A. Milner, and V. Milner, Directional spinning of molecules with sequences of femtosecond pulses, Phys. Rev. A **86**, 063413 (2012).

[37] J. Floß and I. Sh. Averbukh, Molecular spinning by a chiral train of short laser pulses, Phys. Rev. A **86**, 063414 (2012).

[38] G. Karras, M. Ndong, E. Hertz, D. Sugny, F. Billard, B. Lavorel, and O. Faucher, Polarization Shaping for Unidirectional Rotational Motion of Molecules, Phys. Rev. Lett. **114**, 103001 (2015).

[39] E. Prost, H. Zhang, E. Hertz, F. Billard, B. Lavorel, P. Bejot, Joseph Zyss, Ilya Sh. Averbukh, and O. Faucher, Third-order-harmonic generation in coherently spinning molecules, Phys. Rev. A **96**, 043418 (2017).

[40] E. Prost, E. Hertz, F. Billard, B. Lavorel, and O. Faucher, Polarization-based tachometer for measuring spinning rotors, Opt. Express **26**, 31839 (2018).

[41] J. Karczmarek, J. Wright, P. Corkum, and M. Ivanov, Optical Centrifuge for Molecules, Phys. Rev. Lett. **82**, 3420 (1999).

[42] D. M. Villeneuve, S. A. Aseyev, P. Dietrich, M. Spanner, M. Yu. Ivanov, and P. B. Corkum, Forced Molecular Rotation in an Optical Centrifuge, Phys. Rev. Lett. **85**, 542 (2000).

[43] L. Yuan, S. W. Teitelbaum, A. Robinson, and A. S. Mullin, Dynamics of molecules in extreme rotational states, Proc. Natl. Acad. Sci. USA **108**, 6872 (2011).

[44] A. Korobenko, A. A. Milner, and V. Milner, Direct Observation, Study, and Control of Molecular Superrotors, Phys. Rev. Lett. **112**, 113004 (2014).

[45] A. Korobenko, Control of molecular rotation with an optical centrifuge, J. Phys. B **51**, 203001 (2018).

[46] A. A. Milner, J. A. M. Fordyce, I. MacPhail-Bartley, W. Wasserman, V. Milner, I. Tutunnikov, and I. Sh. Averbukh, Controlled Enantioselective Orientation of Chiral Molecules with an Optical Centrifuge, Phys. Rev. Lett. **122**, 223201 (2019).

[47] H. Goldstein, *Classical Mechanics* (Addison Wesley, San Francisco, CA, 2002).

[48] L. D. Landau and E. M. Lifshitz, *Mechanics*, 3rd ed. (Butterworth-Heinemann, Oxford, 1976).

[49] M. J. Frisch, G. W. Trucks, H. B. Schlegel, G. E. Scuseria, M. A. Robb, J. R. Cheeseman, G. Scalmani, V. Barone, G. A. Petersson, H. Nakatsuji, X. Li, M. Caricato, A. V. Marenich, J. Bloino, B. G. Janesko, R. Gomperts, B. Mennucci, H. P. Hratchian, J. V. Ortiz, A. F. Izmaylov *et al.*, GAUSSSIAN 16, Rev. A.03 (2016).

[50] D. C. Rapaport, *The Art of Molecular Dynamics Simulation*, 2nd ed. (Cambridge University Press, Cambridge, England, 2004).

[51] R. Zare, *Angular Momentum: Understanding Spatial Aspects in Chemistry and Physics* (Wiley, New York, 1988).

[52] P. M. Felker, Rotational coherence spectroscopy: Studies of the geometries of large gas-phase species by picosecond time-domain methods, J. Phys. Chem. **96**, 7844 (1992).

[53] S. Keshavamurthy and P. Schlagheck, *Dynamical Tunneling: Theory and Experiment* (CRC Press, Boca Raton, FL, 2011).

[54] W. G. Harter and C. W. Patterson, Rotational energy surfaces and high-J eigenvalue structure of polyatomic molecules, J. Chem. Phys. **80**, 4241 (1984).

[55] E. F. Thomas, A. A. Søndergaard, B. Shepperson, N. E. Henriksen, and H. Stapelfeldt, Hyperfine-Structure-Induced Depolarization of Impulsively Aligned I_2 molecules, Phys. Rev. Lett. **120**, 163202 (2018).

[56] H. H. Ku, Notes on the use of propagation of error formulas, J. Res. Nat. Bur. Stand. Sec. C: Eng. Inst. **70C**, 263 (1966).

[57] T. R. Bott and H. N. Sadler, Vapor pressure of propylene oxide, J. Chem. Eng. Data **11**, 25 (1966).

[58] G. L. Kamta, A. D. Bandrauk, and P. B. Corkum, Asymmetry in the harmonic generation from nonsymmetric molecules, J. Phys. B **38**, L339 (2005).

[59] E. Frumker, C. T. Hebeisen, N. Kajumba, J. B. Bertrand, H. J. Wörner, M. Spanner, D. M. Villeneuve, A. Naumov, and P. B. Corkum, Oriented Rotational Wave-Packet Dynamics Studies Via High Harmonic Generation, Phys. Rev. Lett. **109**, 113901 (2012).

[60] E. Frumker, N. Kajumba, J. B. Bertrand, H. J. Wörner, C. T. Hebeisen, P. Hockett, M. Spanner, S. Patchkovskii, G. G. Paulus, D. M. Villeneuve, A. Naumov, and P. B. Corkum, Probing Polar Molecules with High Harmonic Spectroscopy, Phys. Rev. Lett. **109**, 233904 (2012).

[61] P. M. Kraus, D. Baykusheva, and H. J. Wörner, Two-Pulse Field-Free Orientation Reveals Anisotropy of Molecular Shape Resonance, Phys. Rev. Lett. **113**, 023001 (2014).

[62] H. Harde, S. Keiding, and D. Grischkowsky, THz Commensurate Echoes: Periodic Rephasing of Molecular Transitions in Free-Induction Decay, Phys. Rev. Lett. **66**, 1834 (1991).

[63] S. Fleischer, Y. Zhou, R. W. Field, and K. A. Nelson, Molecular Orientation and Alignment by Intense Single-Cycle THz Pulses, Phys. Rev. Lett. **107**, 163603 (2011).

[64] P. Babilotte, K. Hamraoui, F. Billard, E. Hertz, B. Lavorel, O. Faucher, and D. Sugny, Observation of the field-free orientation of a symmetric-top molecule by terahertz laser pulses at high temperature, Phys. Rev. A **94**, 043403 (2016).

[65] E. Gershnabel and I. Sh. Averbukh, Electric deflection of rotating molecules, J. Chem. Phys. **134**, 054304 (2011).

[66] E. Gershnabel and I. Sh. Averbukh, Deflection of rotating symmetric top molecules by inhomogeneous fields, J. Chem. Phys. **135**, 084307 (2011).

[67] A. Yachmenev, J. Onvlee, E. Zak, A. Owens, and J. Küpper, Field-induced diastereomers for chiral separation, arXiv:1905.07166.

[68] S. Fleischer, Y. Khodorkovsky, E. Gershnabel, Y. Prior, and I. Sh. Averbukh, Molecular alignment induced by ultrashort laser pulses and its impact on molecular motion, Isr. J. Chem. **52**, 414 (2012).

[69] M. Lemeshko, R. V. Krems, J. M. Doyle, and S. Kais, Manipulation of molecules with electromagnetic fields, Mol. Phys. **111**, 1648 (2013).

[70] Y.-P. Chang, D. A. Horke, S. Trippel, and J. Küpper, Spatially-controlled complex molecules and their applications, Int. Rev. Phys. Chem. **34**, 557 (2015).

[71] I. Tutunnikov, J. Floß, E. Gershnabel, P. Brumer, I. Sh. Averbukh, A. A. Milner, and V. Milner (unpublished).

[72] P. P. Man, Cartesian and spherical tensors in NMR Hamiltonians, Concepts Magn. Reson. Part A **42**, 197 (2013).